Packing properties and steady strength of cemented loose granular materials

David Cantor[a,b,*], Carlos Ovalle[a,b]

[a] *Department of Civil, Geological and Mining Engineering, Polytechnique Montreal, Montreal, QC, Canada*
[b] *Research Institute of Mining and Environment, RIME UQAT-Polytechnique, Montreal, QC, Canada*

Abstract

We study samples composed of loose cemented assemblies of particles under isotropic compression and biaxial shearing by means of a discrete-element approach. Compression tests are undertaken by consolidation of grains initially not presenting contacts under varying level of cementation and increasing confining pressure. We find a nonlinear evolution of the solid fraction with pressure that is described using the evolution of granular connectivity and the collapse of pores under homogeneous load. The poral space is characterized in terms of probability of void size number and volume distribution which, surprisingly, can contain voids as 30 times the size of an average particle. Under steady flow, the shear strength turned out to evolve non linearly with the cementation level. For cementation strengths below the confining pressure, the cementation between particles has little effect upon macroscopic friction angle. For greater values of cementation, a rapid increase of macroscopic friction occurs despite a drop in grain connectivity. Macroscopic cohesion is, in turn, small when compared with the interparticle bonding strength for highly cemented samples. The increment of macroscopic strength is found to deeply depend on the anisotropy of contact forces despite a homogeneous distribution of contact orientations and lower connectivity for highly cemented samples.

Keywords: cementation, discrete element method, compaction, shear

*Corresponding author
Email addresses: david.cantor@tpolymtl.ca (David Cantor), carlos.ovalle@polymtl.ca (Carlos Ovalle)

strength, loose granular material

1. Introduction

Cemented soils consist in assemblies of glued particles by bonding agents which may be of natural origin or artificially added into the soil. These geomaterials can be formed by mixtures of granular and cohesive soils, such as sandy clays and silts, but also exclusively by bonded sand grains (Mitchell and Soga, 2005). In natural sedimentary and residual cemented soil deposits, bonding is usually attributed to silicates and carbonates (Clough et al., 1981; Huang and Airey, 1998). For instance, calcareous sands commonly present natural cementation due to precipitation of calcium carbonate (Coop and Atkinson, 1993). Similarly, synthetic silty mine tailings can present weak cementation due to iron oxidation (Robertson et al., 2019). On the other hand, artificial cementation with Portland cement, gypsum or lime, is also used to increase stiffness and strength of compressible and weak soils. Common cementation techniques are based on cement addition in soil mixtures before compaction (Rosa et al., 2008; Consoli et al., 2007; Ismail et al., 2002; Marques et al., 2021), cement grout injection (Kaga and Yonekura, 1991; Karol, 2005), and - more recently - bacterial activity has been used to generate microbially induced calcite precipitation that cements sand grains (DeJong et al., 2006; Cui et al., 2017).

Due to their singular properties (compared to conventional cohesive or granular soils), the mechanical response of cemented soils has attracted significant attention from practitioners and researchers (Schnaid et al., 2001; Wang and Leung, 2008; Consoli et al., 2009). Cementation provides arching of clusters formed by bonded grains, eventually maintaining a loose state even at high effective stresses (Coop and Airey, 2003). Bonding generates a particular microstructure that characterizes the mechanical behavior of the soil, with relatively high shear strength, high sensitivity, and apparent overconsolidation pressure. In general, cementation leads to brittle behavior under shearing, followed by yielding, softening, and strain localization (Leroueil and Vaughan, 1990; Estrada et al., 2010a). Several studies have shown that shear strength increases with the degree of cementation, i.e., both macroscopic cohesion and friction angle increase (Clough et al., 1981; Wang and Leung, 2008; Consoli et al., 2009). While one might expect that interparticle bonding logically results in higher macromechanical cohesion,

the source of frictional strength is not well understood and the answer may lie at the micromechanical scale.

Several authors have used discrete-element methods (DEM) to examine the behavior of cemented soils at the particle scale, using wide ranges of cementation degrees and material properties (Jiang et al., 2011; Shen et al., 2016; Estrada et al., 2010b). These works have allowed for a better understanding of the relationship between the amount of bonding, breakage, and yielding, as well as they have revealed detailed observations of shear band formation. In general, implementing bonds between grains in DEM models allows one to capture the features of the mechanical behavior of cemented sands.

Based on shearing tests using DEM simulations, Ning et al. (2017) showed that the anisotropies of contact orientations and interparticle force orientations significantly increase with the degree of cementation. In other words, in highly cemented sheared samples, strong force chains appear along the axis of deviatoric loading. Conversely, in lightly cemented specimens the material can easily experience local shear rearrangement and force redistribution, thus developing lower strength compared to more cemented samples. Jiang et al. (2013) proposed that the increasing of friction angle with the degree of cementation is due to intact bonds remaining at failure, which generates clusters of irregular shape with high rolling resistance (interlocking), thus increasing the macromechanical shear strength. However, a deep micromechanical analysis involving a large range of bonding degrees, material densities and mean pressures, could significantly contribute to a better understanding on these poorly studied mechanisms. Moreover, a comprehensive study of packing properties depending on cementation strength and the development of grain agglomeration could improve the knowledge on natural cemented soil formation and give insights on the properties of artificially cemented soil specimens.

The main objective of this paper is to study the effect of interparticle bonding (i.e., level of cementation) on packing properties, compressibility, and strength of loose cemented granular assemblies under biaxial shearing. We developed numerical DEM simulations of 2D granular materials over a large range of cementation strengths. Samples are generated by random agglomeration of unsettled grains, resulting in looser states for high bonding strengths. Samples are subjected to a large range of mean pressures and then sheared until a steady state quasi-static regime is reached. We analyze the results for different levels of cementation based on a scaling parameter

depending only on the ratio between bonding strength and mean pressure. Microstructural observations of void distribution and connectivity, as well as micromechanical analysis of contacts and force distributions and orientations, allow us to identify the sources of shear strength in cemented loose granular media.

This paper is organized as follows. In Sec. 2, we present the numerical procedures to create loose grain arrangements, and the characteristics of the compression and shear tests in the frame of the discrete-element modeling. In Sec. 3, we characterize the properties of loose samples after compression under a wide range of pressures and interparticle cementation strengths. Finally, in Sec. 4, we present the steady shear strength of the samples and its relation with microstructural parameters using the granular stress tensor and a well-known decomposition of stresses via anisotropies. This analysis leads to a description of the limit states (failure envelope) of bonded loose granular media as a function of the cementation level and the confining pressure. Finally, we present some conclusions and perspectives.

2. Construction of samples

Loose cohesive samples are built using a discrete-element approach called contact dynamics (CD) (Dubois et al., 2018; Jean, 1999; Renouf et al., 2004). The CD is non-smooth implicit strategy that considers collections of bodies having steric and friction/cohesive interactions. The body velocities and impulses (i.e., changes in momentum) are computed in a time-stepping scheme by integrating the motion equation under the constraints added by the contact between bodies. We can then find the average contact forces during a time step by simply dividing the impulses found between paris of bodies in contact by the time step. For this work, we used the simulation platform LMGC90 (Dubois et al., 2011, 2020) in which the CD method is implemented.

To build controlled loose cohesive samples, we use circular grains in 2D with average diameter $\langle d \rangle$ and a small size variability around such value, so $d_{max}/d_{min} = 1.5$. The particle sizes are uniformly distributed by volume fractions between these two limits. $N_p = 5000$ particles are initially placed in a square grid with a separation between grains of $2d_{max}$. Using four rigid walls around the assembly, we are capable to impose an isotropic or biaxial shearing on the grains. Different sample configurations are produced by adding a cohesive interaction force f_c and, then, letting the particle rattle and agglomerate. The rattling motion of the particles is set by using an

initial random velocity in the range $[0, v_r]$, pointing at a random orientation between $[0, 2\pi]$ radians. The velocity v_r needs to be set considering that the total kinetic energy of the particles remains above the energy being injected by the motion of the walls. This ensures that neither the granular system will create many clusters that the walls will crush before finding equilibrium nor the walls will gain too much inertia that will dynamically damage the clustering of bodies. The cohesive force between bodies is only activated when the gap between them is smaller than the distance $\delta < 0.05\langle d \rangle$. At the contact point between two disks, the force acts simultaneously in the normal and tangential orientations of the interaction providing tensile and shear strength to mimic a solid cementation. With f_c being a constant bonging force, the typical bonding strength at the grain scale can be written as $\sigma_c = f_c/\langle d \rangle$.

Our samples were built varying the relative level of cementation

$$\tilde{C} = \sigma_c / P, \tag{1}$$

in the range $[0, 3 \times 10^2]$, with P the confining pressure. In other words, we created samples varying from non cohesive to strongly cohesive. For convenience, for each level of f_c three different confining pressures were applied. Under the isotropic pressure P, a steady compact stage was defined once the solid fraction $\nu = V_s/V$ (where V_s is the total volume (surface) of the particles, and V the volume of the box), and the coordination number $Z = 2N_c/N_p$ (where N_c is the number of contacts) presented only small fluctuations under the 0.01% over an average value for each value of $\tilde{C}$. During this compression, the bonding force between the bodies is permanent and reversible. This means that a broken interaction can be regained if the gap between the bodies is again smaller that δ. In Fig. 1, we can observe screenshots for a non cohesive and a very cohesive sample after stabilization. We can see that, as the cementation level increases, looser configurations are produced as the bonds are capable to create mechanically stable macro-pores of varying sizes.

3. Packing properties

The mechanical stability after compression produces distinctive structures with evolving solid fraction, pore size distribution, and connectivity. Figure 2 presents the evolution of solid fraction for increasing cementation level between particles. The evolution of ν is nonlinear and presents small variations

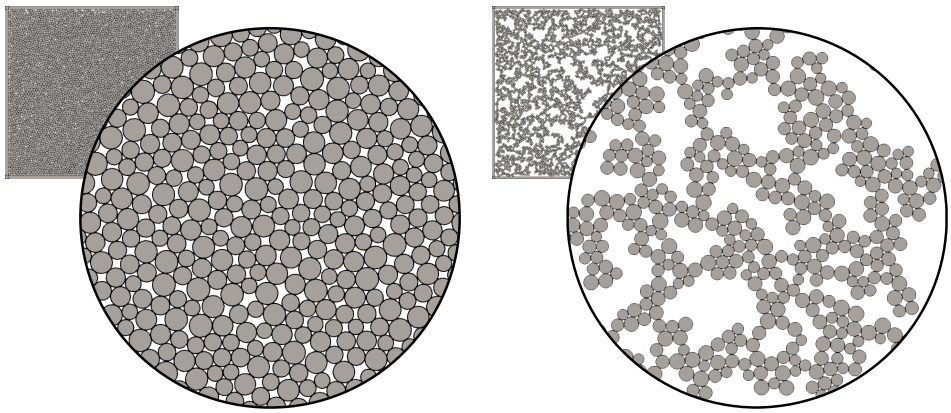

(a) (b)

Figure 1: Screenshots of (a) non cemented (i.e, $\tilde{C} = 0$) and (b) strongly cemented samples (i.e., $\tilde{C} = 3 \times 10^2$).

for values of $\tilde{C}$ lower than 1. As the cementation strength reaches values greater than the confining pressure (i.e., $\tilde{C} > 1$), the solid fraction rapidly drops to values as small as $\simeq 0.5$. The asymptotic trend of ν for large $\tilde{C}$ suggests that a critical value of minimal solid fraction can be reached with this consolidation procedure.

The distribution of pore sizes is also a relevant parameter since it is related to the permeability of the assembly and the potential of collapse. In two-dimensional simulations, as pores are enclosed areas by series of particles in contact, we used an approach known as 'Connected-Component Labeling (CCL)' to identify the different pores in the samples (He et al., 2009). Once the connected regions (voids) are identified, it is straightforward to find their respective size distribution. Figure 3(a) presents the probability density function of number of pores with size V_v, normalized by the size of an average particle $\langle V_d \rangle$, for increasing relative cementation level. We can observe that, initially, the non cohesive sample predominately presents small pores, and the probability of finding bigger pores decays exponentially with V_v. Once the grains have higher bonding strengths and looser stable states are reachable, the peak of the distribution moves to slightly bigger pore sizes - around 10% of V_d - but keep presenting a exponential decay for bigger pore sizes.

In highly cemented samples, it is also natural to find a significant proportion of small pores but, as we could observe in a previous visualization,

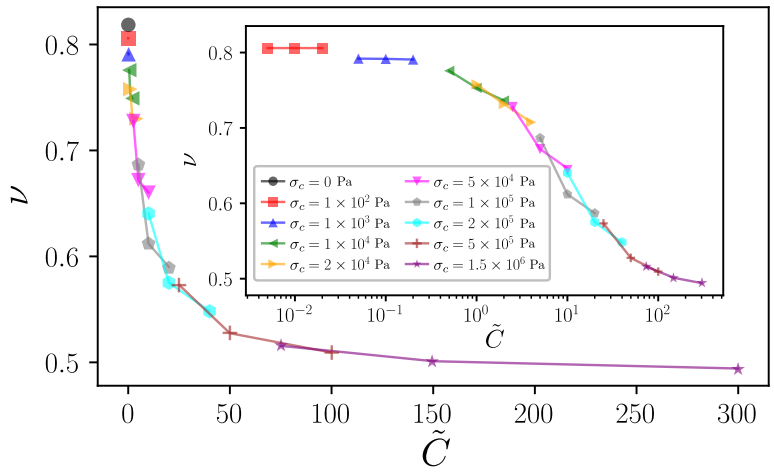

Figure 2: Evolution of the solid fraction ν as a function of the relative level of cementation $\tilde{C} = \sigma_c/P$. In the inset, the same data is presented in log-lin scale.

big pores can indeed be several times bigger that an average particle size. To better account for the pore volumes, Fig. 3(b) shows the cumulative pore size as a function of V_v. In this figure, the distributions gradually shift to the right of the plot as bigger pores are found in the samples, which, besides, can reach volumes as big as ~ 30 times the volume of an average particle.

The capability of the samples to create larger pores is directly linked to a decay of grain connectivity. We observed that the coordination number also evolves non-linearly with the cementation level as shown in Fig. 4. For the non-cemented or weakly cemented samples, the coordination number is found, as expected, near 4 (Bideau and Troadec, 1984; Voivret et al., 2007). But as soon as $\tilde{C} > 1$, Z gradually decreases and, for large values of cementation, the coordination number asymptotically tends to a value slightly larger than 3. While the upper bound of the coordination number is known for randomly non cohesive particle assemblies, the lower bound, on the other hand, depends on the additional stability the bonding forces add to the system. Nonetheless, we find that the relation between the evolution of connectivity and solid fraction can be well captured by a power-law (see inset of Fig. 4) in the form:

$$(Z_0 - Z) = \alpha(\nu_0 - \nu)^\beta, \tag{2}$$

with Z_0 and ν_0 being the coordination number and the solid fraction, respec-

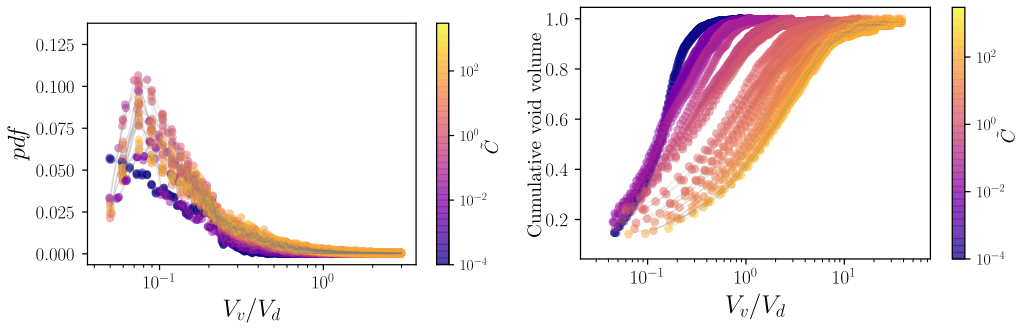

Figure 3: (a) Probability density function of pore sizes V_v by number and (b) proportion of cumulative void volume for increasing relative cementation strength $\tilde{C}$.

tively, for the non cohesive sample $\tilde{C} = 0$. This relation has experimentally been studied in the past, and several empirical equations have been attributed to these parameters for loose granular configurations (Oda, 1977). We find that the parameters of the power-law that best fit our data are $\alpha \simeq 4.5$ and $\beta \simeq 1.8$. The nature of these constants α and β are interesting since the relation Z vs. ν has also been found to follow a power-law distribution for non cohesive systems with similar coefficients (Durian, 1995; Katgert and van Hecke, 2010; Cantor et al., 2020b). This work confirms, once again, the existence of a correlation $Z - \nu$ under a power-law relation underlying this intrinsic property of granular media.

In order to better describe the relations $P-\nu-Z$, let us consider the granular stress tensor as $\sigma_{ij} = n_c\langle f_i \ell_j \rangle$ (Ouadfel and Rothenburg, 2001; Rothenburg and Bathurst, 1989), where $n_c = N_c/V$ is the volumetric density of contacts, and $\langle \ldots \rangle$ the average of the product of contact forces f and branch vectors ℓ (i.e., the vectors joining the center of mass of particles in contact). Taking the mean pressure on the assemblies as $P = (\sigma_1 + \sigma_2)/2$, with σ_1 and σ_2 being the principal values of tensor σ, we can write an expression for the pressure on the sample as a function of structural parameters as (Agnolin and Roux, 2007; Azéma et al., 2018)

$$P = \frac{Z\nu f^*}{\pi\langle d \rangle}, \tag{3}$$

where f^* is a typical force between the particles. The force f^* is challenging to assess because, in the one hand, it should introduce the asymptotic behavior

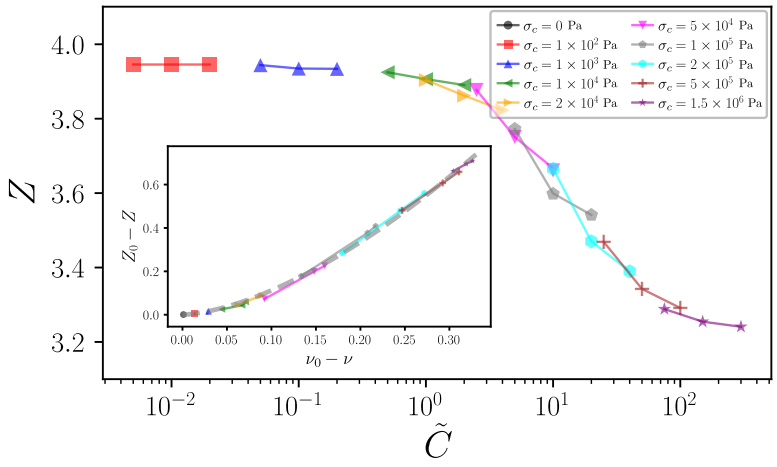

Figure 4: Evolution of the coordination number Z as a function of the relative cementation level $\tilde{C}$. In the inset, we present the reduced coordination number as a function of the reduced solid fraction with Z_0 and ν_0 the coordination number and solid fraction, respectively, for the non cemented case $\tilde{C} = 0$.

observed towards either low or high relative cementation $\tilde{C}$. On the other hand, the relation $f^*/\langle d \rangle$ is expected to translate the averaged stress states for the whole set of grains which is impossible to make through experimental approaches.

Despite this, the compression of loose granular assembly can be considered a coupled mechanical-geometrical problem in which the pores are filled by the deformation of stable mesostructures (aggregates of particles) by the action of an increasing external isotropic pressure. To provide a solution to this process, we can use an approached based on analytical elastic solutions for the collapse of cavities within spheres under homogeneous pressures (Carroll and Kim, 1984). Under such analogy, a logarithmic relation yields in the form: $f^*/\langle d \rangle = -A \log\{(\nu_0 - \nu)/(\nu_0 - \nu_{min})\}$, where ν_{min} is the lower bound of solid fraction as $\tilde{C} \gg 1$, and A is a constant. This relation is expected to be affected by the cementation force as an intrinsic force intensity at the contact level, so A should scale as $bf_c/\langle d \rangle$, with b a proportionality factor. Then, also using Eq. (2), we can write a compression equation for our loose granular systems as

$$\frac{1}{\tilde{C}} = -\frac{b\{Z_0 - \alpha(\nu_0 - \nu)^\beta\}\nu}{\pi} \log\left\{\frac{\nu_0 - \nu}{\nu_0 - \nu_{min}}\right\}. \tag{4}$$

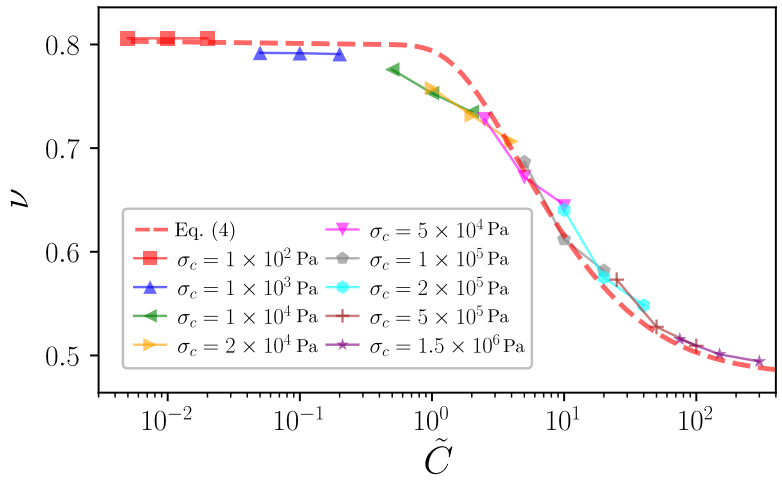

Figure 5: Evolution of the solid fraction as a function of the relative level of cementation (as in Fig. 2) along with Eq. 4 shown with a dashed red line.

From this relation, we can observe that constant b can be understood as the a compressibility coefficient characterizing the transition between the two limit states from poorly cemented to strongly cemented configurations.

Simple fitting of this relation to the data presented in Fig. 2 reveals that $\nu_{min} \simeq 0.48$ and $b \simeq 0.2$. Figure 5 shows the same data as in Fig. 2 and the excellent fitting Eq. (4) produces over more than 4 decades of cementation level $\tilde{C}$.

4. Shear strength

To characterize the shear strength of cemented loose samples, we modified the contact law used for the isotropic compression, so only the set of contacts at the beginning of the simulation are considered cemented. Once these contacts are lost either by tensile or shear forces reaching the threshold f_c, they can not be recovered and new interactions between particles are considered dry frictional with coefficient of friction $\mu = 0.4$.

The shearing tests are performed under biaxial configuration by applying a constant velocity v on the upper and lower walls and a constant pressure on the lateral walls (i.e., the same pressure P applied for the isotropic compression). The velocity of the walls was simply set to obey quasi-static conditions so the inertial number $I = \dot{\varepsilon_v}\langle d\rangle\sqrt{\rho/P} \ll 1$, where $\dot{\varepsilon_v} = v/h_0$ is the vertical

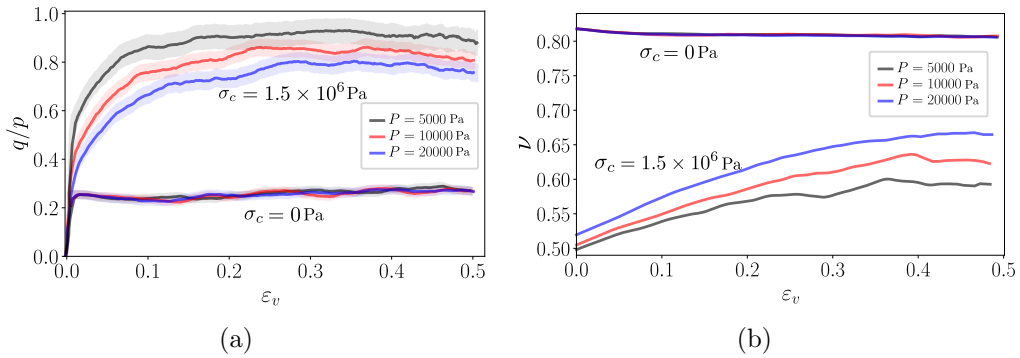

Figure 6: Evolution of the ratio q/p (a) and the solid fraction ν (b) as a function of the vertical deformation ε_v for the non-cemented and a very cemented samples.

strain rate, h_0 is the initial height of the sample, and ρ the grains' density. The tests are undertaken up to a cumulative vertical strain $\varepsilon_v = 50\%$.

We used the granular stress tensor (presented in the previous section), to find the mean pressure during shearing as $p = (\sigma_1 + \sigma_2)/2$ and deviatoric stress $q = (\sigma_1 - \sigma_2)/2$. Figure 6(a) presents the evolution of the ratio q/p for the samples with $\tilde{C} = 0$ (i.e., the non-cemented sample), and $\tilde{C} = 3{\times}10^2$ (i.e., the sample with the strongest cementation among our tests), for different levels of lateral pressure applied. For the non-cemented case, the samples rapidly reach a steady strength that, as expected, is independent of the confining pressure. For the very cemented and loose case, the evolution of q/p is more gradual and after $\varepsilon_v \simeq 0.25$ the strength reaches a steady value. Note that no peak of strength is observed given that the initial configurations of the samples is loose. Figure 6(b) presents the evolution of the solid fraction towards a steady state density. Such plateau of solid fraction is rapidly reached for poorly cemented samples. But as f_c increases, the evolution of ν is slower and we can only consider that a steady value is reached after $\varepsilon_v \simeq 0.45$. We then extracted all values of q, p, and ν (averaged) at the level of deformation considered to be at the steady regime for each sample.

Figure 7(a) gathers the steady values of q and p for each value of cementation between particles and the different confining pressures. Following the Mohr-Coulomb failure criterion as

$$\frac{q}{p} = \sin(\phi) + \frac{c}{p}\cos(\phi), \tag{5}$$

each set of three tests per sample allows to extract the macroscopic coeffi-

cient of friction ϕ and cohesion c. In the same plot, Figs. (b) and (c) gather the resistance parameters as the cementation strength σ_c increases. We can observe that the macroscopic coefficient of friction $\sin(\phi)$ is practically independent of the cementation between particles as far as the confining pressure is higher than the cementation strength σ_c. Once the cementation level is more relevant than the confining pressure, the macroscopic friction rapidly increases up to $\sin(\phi) \simeq 0.7$ or $\phi \simeq 40°$. The macroscopic cohesion also increases with σ_c. Nonetheless, when presented under the normalization c/σ_c (inset of Fig. 7(c)), we notice its value decreases which demonstrates that the increase in the bonding force between particles is relatively less important when translated to the macroscale. The combined behavior of macroscopic friction and cohesion can be understood given the formation of larger pores of less connected particles along with the increase of cementation. As σ_c increases, larger pores create rougher local textures that can promote additional shear resistance.

The evolution of strength and scaling up of cohesive bonds depends as well on the proportion of bonds that are broken during shear and replaced either by 'sliding' contacts (i.e., interactions in which the Coulomb dry friction is mobilized) or 'stick' contacts, in which the Coulomb threshold has not been reached. Figure 8 presents the evolution of the proportion of cemented, sliding, and stick contacts for two different levels of cementation $\tilde{C}$ as a function of the vertical deformation ε_v. We can corroborate the little influence of the cementation has at the steady state for values of $\tilde{C}$ below 1 given the continuous breakage of cemented bonds (see Fig. 8(a)). At the same time, for cementation levels beyond 1, the cementation is not lost as fast as for low $\tilde{C}$ (see Fig. 8(b)). Nonetheless, an intricate coupling coordination-breakage of bonds, lets us deduce that a more 'steady' set of broken and sliding contacts is supporting the stability of strength while some cemented clusters are being mobilized as blocks. It is also interesting to remark that, despite a continuous evolution in the proportion of contact types for large level of strain, the macroscopic strength and solid fraction present steady values as early as for $\varepsilon_v \simeq 5\%$. This points out the different stabilization time (or deformation) scales differing from macroscopic behavior and microscopic structure.

The combinations of stresses q and p found at the steady state define a failure envelope which evolves in terms of the cementation level. By plotting the ratio q/p as a function of $\tilde{C}$, as in Fig. 9, we can observe the non-linear evolution of limit states for our set of loose samples. The lower bound of the curve corresponds to the non cemented configuration which spans from

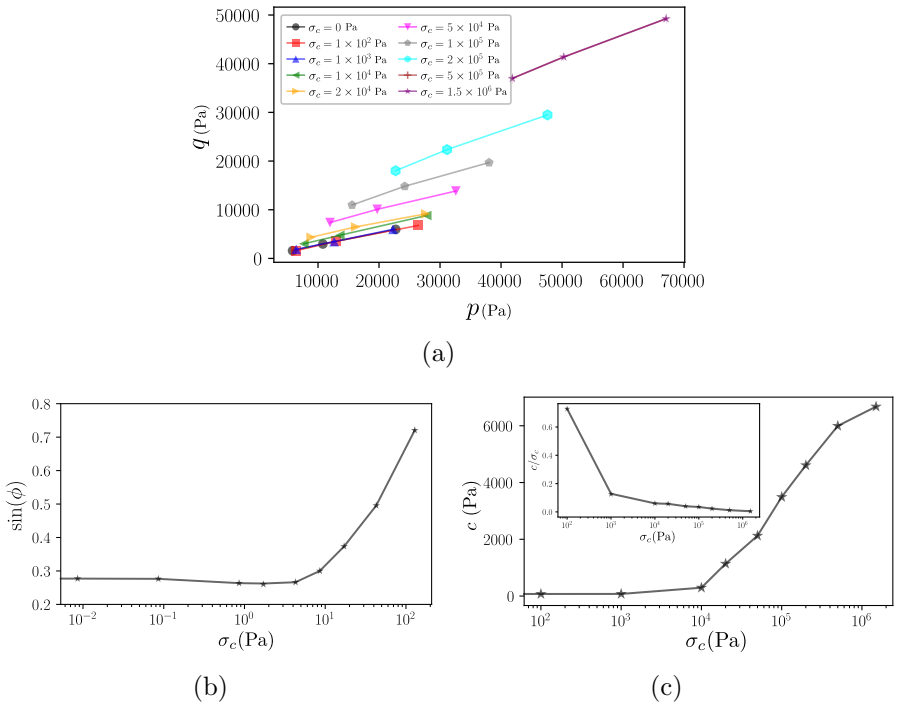

Figure 7: (a) Average values of deviatoric stress q and mean pressure p for the different levels of cementation and three different confining pressure per sample. (b) Macroscopic coefficient of friction as a function of the cementation level normalized by the average confining pressure at consolidation and mean diameter of the grains. (c) Macroscopic cohesion c as a function of cementation strength. In the inset we present the same data but c appears normalized by σ_c.

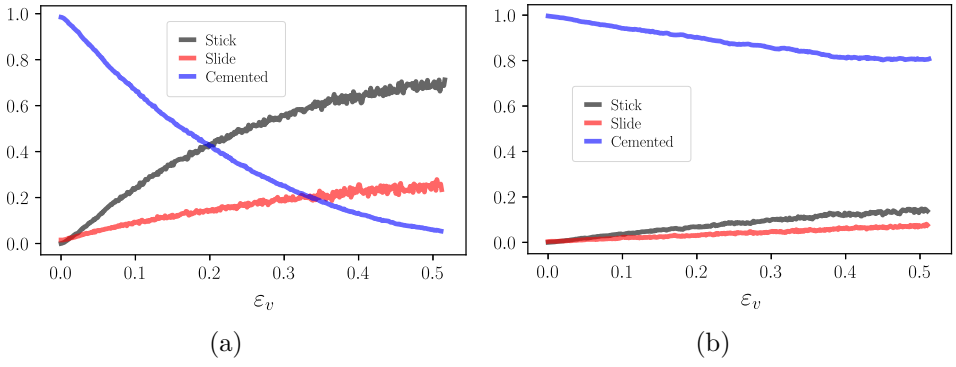

Figure 8: Evolution of the proportion of different contact types as a function of the deformation for the sample with (a) $\tilde{C} = 1 \times 10^{-2}$ and (b) $\tilde{C} = 2 \times 10^{1}$

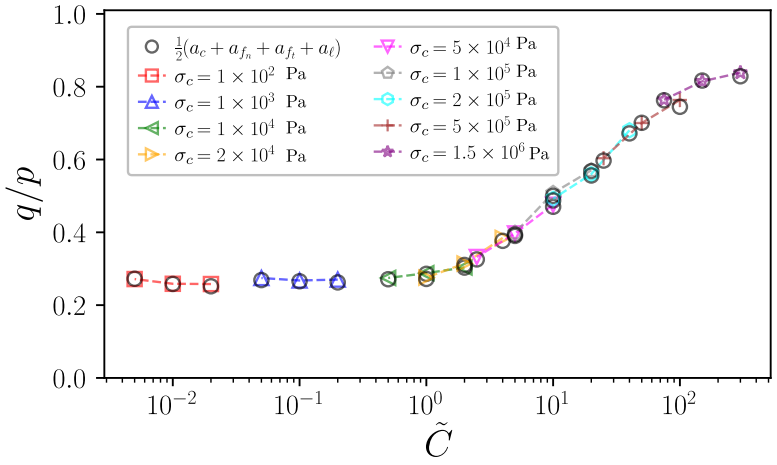

Figure 9: Evolution of limit states in the space q/p as a function of the cementation level $\tilde{C}$.

$\tilde{C} = 0$ to $\tilde{C} \simeq 1$. After such a value, the limit state gradually reaches higher values of q/p and end up asymptotically trending to a value ~ 0.85.

For circular and monodispersed particles, the shear strength q/p can be easily characterized using microstructural parameters linked to the geometrical organization of the grains and the force transmission. For this micromechanical analysis, we need first to define a contact frame for each interaction particle-particle. Let $\boldsymbol{n}$ and $\boldsymbol{t}$ represent the unitary normal and tangential vectors, respectively, of the interaction, so the vector total force can be defined as $\boldsymbol{f} = f_n\boldsymbol{n} + f_t\boldsymbol{t}$, with f_n and f_t the normal and tangential components of the force. In addition, the branch vectors (i.e., the vectors joining the center of mass of touching particles) are defined as $\boldsymbol{\ell} = \ell\boldsymbol{n}$ whose norm is ℓ and, for circular grains, are orientated along with vector $\boldsymbol{n}$. Thus, it is possible to rewrite the stress tensor in terms of angular distributions of contact forces and branch vectors and deduce an expression of the shear strength as (Rothenburg and Bathurst, 1989; Yimsiri and Soga, 2010; Azéma and Radjai, 2010; Guo and Zhao, 2013; Cantor et al., 2020a)

$$\frac{q}{p} \simeq \frac{1}{2}\{a_c + a_{f_n} + a_{ft} + a_\ell\}, \tag{6}$$

where a_c is the anisotropy of contact orientations, a_ℓ is the anisotropy of branch lengths, and a_{f_n} and a_{f_n} are the anisotropies of the normal and tangential forces, respectively. These anisotropies are easily obtained using the

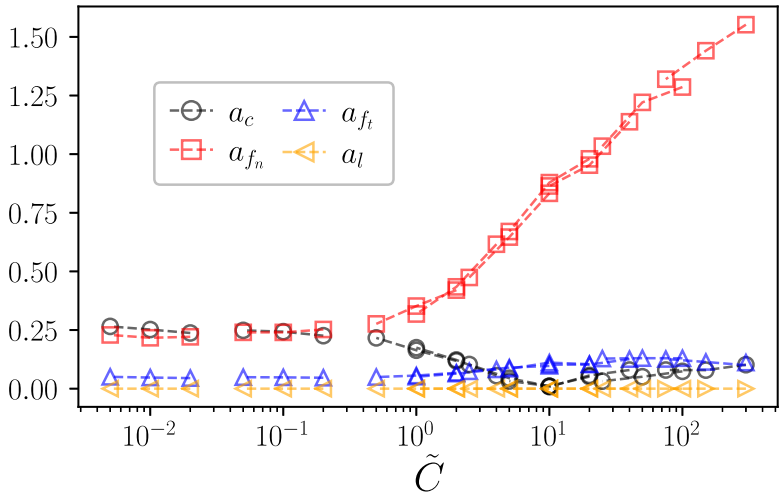

Figure 10: Evolution of the different microstructural anisotropies as a function of the cementation level at the steady state.

fabric tensor $F_{ij} = 1/N_c \sum_{\forall c} n_i n_j$, with n the unitary normal vector, so $a_c = 2(F_1 - F_2)$ with F_1 and F_2 being the eigenvalues of F_{ij}; the normal forces tensor $\chi_{ij}^{f_n} = 1/N_c \sum_{\forall c} f_n n_i n_j$, so $a_{f_n} = 2(\chi_1^{f_n} - \chi_2^{f_n})/(\chi_1^{f_n} + \chi_2^{f_n})$, where $\chi_1^{f_n}$ and $\chi_2^{f_n}$ are the eigenvalues of $\chi_{ij}^{f_n}$; the tangential forces tensor $\chi_{ij}^{f_t} = 1/N_c \sum_{\forall c} f_t n_i n_j$, with which we build the tensor $\chi_{ij}^{f} = \chi_{ij}^{f_n} + \chi_{ij}^{f_t}$ and compute $a_{f_t} = 2(\chi_1^{f} - \chi_2^{f})/(\chi_1^{f} + \chi_2^{f})$ using χ_1^{f} and χ_2^{f}, the eigenvalues of χ_{ij}^{f}; and the branch tensor $\chi_{ij}^{\ell} = 1/N_c \sum_{\forall c} \ell n_i n_j$, so $a_\ell = 2(\chi_1^{\ell} - \chi_2^{\ell})/(\chi_1^{\ell} + \chi_2^{\ell})$, where χ_1^{ℓ} and χ_2^{ℓ} are the eigenvalues of χ_{ij}^{ℓ}.

In the same Fig. 9, we plot the shear strength using the anisotropies as in Eq. (6) using empty black dots proving the accuracy of the microscopic decomposition of the shear strength. Then, in Fig. 10, we observe the different anisotropies and their evolution as $\tilde{C}$ increases.

First, we can remark that a_ℓ remains very close to zero, since the length of the branches does not vary much in the almost monodisperse particle size distribution. Note that the anisotropy of tangential forces has also a minor role in the variability of strength.

On the other hand, we see that the contact orientation anisotropy a_c actually decreases with $\tilde{C}$. This trend is unexpected given that denser systems are more connected and supposed to have more interactions supporting the external loads. To visualize this phenomenon, Fig. 11(a) shows the angu-

lar distribution of contacts orientation probability for samples with level of cementation $\tilde{C} = 0$ and $\tilde{C} = 3 \times 10^2$ at level of deformation of $\varepsilon_v = 40\%$. From these visualizations, we can deduce that the biaxial loading promotes an important decrease of contacts in the perpendicular orientation of the loading for $\tilde{C} = 0$. Such effect does not appear in loose and highly cemented samples, in which the probability of having a contact remains very similar for all orientations. Finally, and given the linear relation between q/p and the anisotropies, we see that the important gain of normal force anisotropy a_{f_n} is the main microstructural element supporting the rise of strength at the macroscale. As an illustration, Fig. 11(b) presents screenshots of the force networks for cases $\tilde{C} = 0$ and $\tilde{C} = 3 \times 10^2$ at a level of deformation $\varepsilon_v = 40\%$. Forces between particles are presented as bars joining the center of mass of the different grains, whose thickness is proportional to the intensity of the force. Tensile forces are presented in blue while compressive forces are red. We can observe that for the non-cemented case, forces are more homogeneously distributed in the sample implying a lower normal force anisotropy. For the very loose cemented case, we note that compressive forces are mostly found in the loading orientation while tensile forces are mostly seen in the horizontal direction. This combined effect supports the rise of a strong anisotropy of forces intensities in the assembly. Besides, the level of cementation $\tilde{C}$ increases, the tensile forces can get values as high as the compressive forces. That large range of forces also backs up the anisotropy of normal forces and, thus, the macroscopic increase of shear strength.

5. Conclusions

In the frame of the discrete-element method, we used two-dimensional circular bodies interacting through a cohesive bonding law to represent samples of cemented grains. By consolidation of grains homogeneously distributed in space and varying the level of bonding force f_c between them and confining pressure P, we were able to build loose samples in the range of solid fractions $\nu \in [0.49, 0.81]$. We observed that the evolution of solid fraction and grain connectivity is non-linear with P. Nonetheless, a power-law relation between solid fraction and coordination number was found reminiscent of the behavior of granular samples compressed beyond jamming. This relation, combined with an analytical approach which describes the collapse of cavities under homogeneous stresses, let us develop a relation between the evolution of the solid fraction as a function of the applied pressure and the level of cementa-

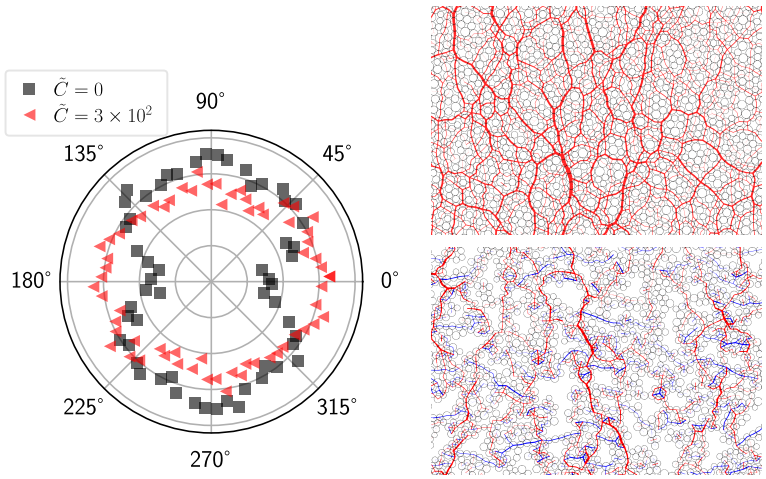

(a) (b)

Figure 11: (a) Evolution of the contact orientation distributions for the non cemented sample $\tilde{C} = 0$ and the sample with largest cementation tested $\tilde{C} = 3 \times 10^2$. (b) Screenshots of the force chains for the same two samples at a vertical deformation $\varepsilon_v = 40\%$. The bars in blue correspond to compressive forces while red bars are tensile forces.

tion between the grains. This approach reproduced very well our numerical results at the same time that allowed us to characterize the configuration of the sample - in terms of solid fraction and connectivity - up to very large values of cementation between grains. We also analysed the pore size distribution by means of a 'connected-component labeling' strategy. This allowed us to observe that that void size decays exponentially independently of the solid fraction and, for the largest value of cementation used in our tests, the size of pores can reach as much as $\simeq 30$ times the typical particle size.

The second part of this work dealt with the shearing strength of the same loose assemblies previously consolidated under isotropic compression. By applying a biaxial quasi-static loading, we reached and characterized the steady state strength of the different samples. First, based on the Mohr-Coulomb failure criterion, we observed that the macroscopic friction angle increases with the level of cementation of the particles despite a lower solid fraction and a reduced connectivity of the grains. The macroscopic values of cohesion, on the other hand, although increasing in absolute values, were less relevant when compared with the local cementation between grains. The increase of shear strength in terms of the ratio q/p was then analysed using a well-known

microstructural decomposition of the stress tensor in terms of contact, forces, and branch anisotropies. This analysis showed that the more tightly packed assemblies are not necessarily those presenting the more homogeneous (less anisotropic) contact network under steady shearing. Loose packings have, indeed, contacts better distributed in all directions despite presenting relatively big pores. We found that the microstructural element that mainly supports the increase of shear strength in cemented loose samples is the anisotropy of the forces in the contact network. This effect is backed-up by the broadening of force ranges that, in the case of very cohesive samples, can present compressive forces as larger as tensile ones. The anisotropy of normal contact forces is clearly observed as columns of compressive forces get aligned with the loading direction while tensile forces are predominately seen in the orthogonal direction to the loading. The anisotropy of tangential forces, on the other hand, has little influence in the overall strength of cemented samples.

Although alternative construction strategies of loose cemented samples can produce slightly different configurations, we presented here a general approach to link compressibility and shear strength characteristics to microstructural and micromechanical elements of granular media. In loose cemented samples, a complex trade-off between cementation strength, less grain connectivity and solid fraction occurs as the confining pressure increases. Nonetheless, force transmission is a mechanism (implicitly involving the geometrical configuration of particles) capable of explaining the shear strength for a large range of cementation levels.

Future works in this vein can add elements to more realistically represent the debonding mechanism and degradation of cemented solid interactions with time or load hysteresis. Those approaches can better reproduce the transition of the samples from static conditions towards plastification and large deformation. Adding more complex particles shape and cemented size polydisperse grains are also key subjects to extend and validate the compression equation and the observations undertaken with simple circular bodies.

Acknowledgements

This research work benefited from the financial support of the Natural Sciences and Engineering Research Council of Canada (NSERC) [Ref. RGPIN-2019-06118], the Fonds de recherche du Québec - Nature et technologies (FRQNT) through the Programme de recherche en partenariat sur le développement durable du secteur minier-II [Ref. 2020-MN-281267] and

the industrial partners of the Research Institute on Mines and the Environment (RIME) UQAT-Polytechnique (irme.ca/en).

References

Agnolin, I., Roux, J.N., 2007. Internal states of model isotropic granular packings. I. Assemblies process, geometry and contact networks. Phys. Rev. E 76, 061302.

Azéma, E., Radjai, F., 2010. Stress-strain behavior and geometrical properties of packings of elongated particles. Phys. Rev. E 81, 051304.

Azéma, E., Sánchez, P., Scheeres, D., 2018. Scaling behavior of cohesive self-gravitating aggregates. Phys. Rev. E 98, 030901(R).

Bideau, D., Troadec, J.P., 1984. Compacity and mean coordination number of dense packings of hard discs. Journal of Physics C: Solid State Physics 17, L731–L735.

Cantor, D., Azéma, E., Preechawuttipong, I., 2020a. Microstructural analysis of sheared polydisperse polyhedral grains. Phys. Rev. E 101, 062901.

Cantor, D., Cárdenas-Barrantes, M., Preechawuttipong, I., Renouf, M., Azéma, E., 2020b. Compaction model for highly deformable particle assemblies. Phys. Rev. Lett. 124, 208003.

Carroll, M.M., Kim, K.T., 1984. Pressure—density equations for porous metals and metal powders. Powder Metallurgy 27, 153–159.

Clough, G.W., Sitar, N., Bachus, R.C., Rad, N.S., 1981. Cemented sands under static loading. Journal of the Geotechnical Engineering Division 107, 799–817.

Consoli, N., da Fonseca, A.V., Cruz, R.C., Heineck, K.S., 2009. Fundamental parameters for the stiffness and strength control of artificially cemented sand. Journal of Geotechnical and Geoenvironmental Engineering 135, 1347–1353.

Consoli, N., Foppa, D., Festugato, L., Heineck, K.S., 2007. Key parameters for strength control of artificially cemented soils. Journal of Geotechnical and Geoenvironmental Engineering 133, 197–205.

Coop, M., Airey, D., 2003. Carbonate sands, in: Characterisation and Engineering Properties of Natural Sands, p. 1049–1086.

Coop, M., Atkinson, J., 1993. The mechanics of cemented carbonate sands. Géotechnique 43, 53–67.

Cui, M.J., Zheng, J.J., Zhang, R.J., Lai, H.J., Zhang, J., 2017. Influence of cementation level on the strength behaviour of bio-cemented sand. Acta Geotechnica 12, 971–986.

DeJong, J., Fritzges, M., Nusslein, K., 2006. Microbially induced cementation to control sand response to undrained shear. Journal of Geotechnical and Geoenvironmental Engineering 132, 1381–1392.

Dubois, F., Acary, V., Jean, M., 2018. The Contact Dynamics method: A nonsmooth story. Comptes Rendus - Mecanique 346, 247–262.

Dubois, F., Jean, M., et al, 2020. LMGC90 wiki page. `https://git-xen.lmgc.univ-montp2.fr/lmgc90/lmgc90_user/wikis/home`. [Online; accessed 17-Jul-2020].

Dubois, F., Jean, M., Renouf, M., Mozul, R., Martin, A., Bagnéris, M., 2011. LMGC90, in: 10e colloque national en calcul des structures, p. 8 p.

Durian, D.J., 1995. Foam mechanics at the bubble scale. Phys. Rev. Lett. 75, 4780.

Estrada, N., Lizcano, A., Taboada, A., 2010a. Simulation of cemented granular materials. i. macroscopic stress-strain response and strain localization. Phys. Rev. E 82, 011303.

Estrada, N., Lizcano, A., Taboada, A., 2010b. Simulation of cemented granular materials. ii. micromechanical description and strength mobilization at the onset of macroscopic yielding. Phys. Rev. E 82, 011304.

Guo, N., Zhao, J., 2013. The signature of shear-induced anisotropy in granular media. Computers and Geotechnics 47, 1–15.

He, L., Chao, Y., Suzuki, K., Wu, K., 2009. Fast connected-component labeling. Pattern Recognition 42, 1977–1987.

Huang, J.T., Airey, D.W., 1998. Properties of artificially cemented carbonate sand. Journal of Geotechnical and Geoenvironmental Engineering 124, 492–499.

Ismail, M., Joer, H., Sim, W., Randolph, M., 2002. Effect of cement type on shear behavior of cemented calcareous soil. Journal of Geotechnical and Geoenvironmental Engineering 128, 520–529.

Jean, M., 1999. The non-smooth contact dynamics method. Computer Methods in Applied Mechanics and Engineering 177, 235–257.

Jiang, M., Yan, H., Zhu, H., Utili, S., 2011. Modeling shear behavior and strain localization in cemented sands by two-dimensional distinct element method analyses. Computers and Geotechnics 38, 14–29.

Jiang, M., Zhang, W., Sun, Y., Utili, S., 2013. An investigation on loose cemented granular materials via DEM analyses. Granular Matter 15, 65–84.

Kaga, M., Yonekura, R., 1991. Estimation of strength of silicate-grouted sand. Soils and Foundations 31, 43–59.

Karol, R., 2005. Chemical Grouting and Soil Stabilization. CRC Press.

Katgert, G., van Hecke, M., 2010. Jamming and geometry of two-dimensional foams. Europhysics Letters 92, 34002.

Leroueil, S., Vaughan, P., 1990. The general and congruent effects of structure in natural soils and weak rocks. Géotechnique 40, 467–488.

Marques, S., Festugato, L., Consoli, N., 2021. Stiffness and strength of an artificially cemented sand cured under stress. Granular Matter 23.

Mitchell, J., Soga, K., 2005. Fundamentals of Soil Behavior, 3rd Edition. John Wiley.

Ning, Z., Khoubani, A., Evans, T.M., 2017. Particulate modeling of cementation effects on small and large strain behaviors in granular material. Granular Matter 19, 1–19.

Oda, M., 1977. Co-Ordination Number and Its Relation To Shear Strength of Granular Material. Soils and Foundations 17, 29–42.

Ouadfel, H., Rothenburg, L., 2001. 'Stress-force-fabric' relationship for assemblies of ellipsoids. Mechanics of Materials 33, 201–221.

Renouf, M., Dubois, F., Alart, P., 2004. A parallel version of the non smooth contact dynamics algorithm applied to the simulation of granular media. Journal of Computational and Applied Mathematics 168, 375–382.

Robertson, P., Melo, L., Williams, D., Wilson, G., 2019. Report of the Expert Panelon the Technical Causes of the Failure of Feijao Dam. Technical Report. Vale S.A.

Rosa, F., Consoli, N., Baudet, B., 2008. An experimental investigation of the behaviour of artificially cemented soil cured under stress. Géotechnique 58, 675–679.

Rothenburg, L., Bathurst, R., 1989. Analytical study of induced anisotropy in idealized granular material. Géotechnique 39.

Schnaid, F., Prietto, P., Consoli, N., 2001. Characterization of cemented sand in triaxial compression. Journal of Geotechnical and Geoenvironmental Engineering 127, 857–868.

Shen, Z., Jiang, M., Thornton, C., 2016. Dem simulation of bonded granular material. part i: Contact model and application to cemented sand. Computers and Geotechnics 75, 192–209.

Voivret, C., Radjai, F., Delenne, J.Y., El Youssoufi, M., 2007. Space-filling properties of polydisperse granular media. Phys. Rev. E 76, 1–12.

Wang, Y., Leung, S., 2008. Characterization of cemented sand by experimental and numerical investigations. Journal of Geotechnical and Geoenvironmental Engineering 134, 992–1004.

Yimsiri, S., Soga, K., 2010. Dem analysis of soil fabric effects on behaviour of sand. Géotechnique 60, 483–495.

References

Agnolin, I., Roux, J.N., 2007. Internal states of model isotropic granular packings. I. Assemblies process, geometry and contact networks. Phys. Rev. E 76, 061302.

Azéma, E., Radjai, F., 2010. Stress-strain behavior and geometrical properties of packings of elongated particles. Phys. Rev. E 81, 051304.

Azéma, E., Sánchez, P., Scheeres, D., 2018. Scaling behavior of cohesive self-gravitating aggregates. Phys. Rev. E 98, 030901(R).

Bideau, D., Troadec, J.P., 1984. Compacity and mean coordination number of dense packings of hard discs. Journal of Physics C: Solid State Physics 17, L731–L735.

Cantor, D., Azéma, E., Preechawuttipong, I., 2020a. Microstructural analysis of sheared polydisperse polyhedral grains. Phys. Rev. E 101, 062901.

Cantor, D., Cárdenas-Barrantes, M., Preechawuttipong, I., Renouf, M., Azéma, E., 2020b. Compaction model for highly deformable particle assemblies. Phys. Rev. Lett. 124, 208003.

Carroll, M.M., Kim, K.T., 1984. Pressure—density equations for porous metals and metal powders. Powder Metallurgy 27, 153–159.

Clough, G.W., Sitar, N., Bachus, R.C., Rad, N.S., 1981. Cemented sands under static loading. Journal of the Geotechnical Engineering Division 107, 799–817.

Consoli, N., da Fonseca, A.V., Cruz, R.C., Heineck, K.S., 2009. Fundamental parameters for the stiffness and strength control of artificially cemented sand. Journal of Geotechnical and Geoenvironmental Engineering 135, 1347–1353.

Consoli, N., Foppa, D., Festugato, L., Heineck, K.S., 2007. Key parameters for strength control of artificially cemented soils. Journal of Geotechnical and Geoenvironmental Engineering 133, 197–205.

Coop, M., Airey, D., 2003. Carbonate sands, in: Characterisation and Engineering Properties of Natural Sands, p. 1049–1086.

Coop, M., Atkinson, J., 1993. The mechanics of cemented carbonate sands. Géotechnique 43, 53–67.

Cui, M.J., Zheng, J.J., Zhang, R.J., Lai, H.J., Zhang, J., 2017. Influence of cementation level on the strength behaviour of bio-cemented sand. Acta Geotechnica 12, 971–986.

DeJong, J., Fritzges, M., Nusslein, K., 2006. Microbially induced cementation to control sand response to undrained shear. Journal of Geotechnical and Geoenvironmental Engineering 132, 1381–1392.

Dubois, F., Acary, V., Jean, M., 2018. The Contact Dynamics method: A nonsmooth story. Comptes Rendus - Mecanique 346, 247–262.

Dubois, F., Jean, M., et al, 2020. LMGC90 wiki page. `https://git-xen.lmgc.univ-montp2.fr/lmgc90/lmgc90_user/wikis/home`. [Online; accessed 17-Jul-2020].

Dubois, F., Jean, M., Renouf, M., Mozul, R., Martin, A., Bagnéris, M., 2011. LMGC90, in: 10e colloque national en calcul des structures, p. 8 p.

Durian, D.J., 1995. Foam mechanics at the bubble scale. Phys. Rev. Lett. 75, 4780.

Estrada, N., Lizcano, A., Taboada, A., 2010a. Simulation of cemented granular materials. i. macroscopic stress-strain response and strain localization. Phys. Rev. E 82, 011303.

Estrada, N., Lizcano, A., Taboada, A., 2010b. Simulation of cemented granular materials. ii. micromechanical description and strength mobilization at the onset of macroscopic yielding. Phys. Rev. E 82, 011304.

Guo, N., Zhao, J., 2013. The signature of shear-induced anisotropy in granular media. Computers and Geotechnics 47, 1–15.

He, L., Chao, Y., Suzuki, K., Wu, K., 2009. Fast connected-component labeling. Pattern Recognition 42, 1977–1987.

Huang, J.T., Airey, D.W., 1998. Properties of artificially cemented carbonate sand. Journal of Geotechnical and Geoenvironmental Engineering 124, 492–499.

Ismail, M., Joer, H., Sim, W., Randolph, M., 2002. Effect of cement type on shear behavior of cemented calcareous soil. Journal of Geotechnical and Geoenvironmental Engineering 128, 520–529.

Jean, M., 1999. The non-smooth contact dynamics method. Computer Methods in Applied Mechanics and Engineering 177, 235–257.

Jiang, M., Yan, H., Zhu, H., Utili, S., 2011. Modeling shear behavior and strain localization in cemented sands by two-dimensional distinct element method analyses. Computers and Geotechnics 38, 14–29.

Jiang, M., Zhang, W., Sun, Y., Utili, S., 2013. An investigation on loose cemented granular materials via DEM analyses. Granular Matter 15, 65–84.

Kaga, M., Yonekura, R., 1991. Estimation of strength of silicate-grouted sand. Soils and Foundations 31, 43–59.

Karol, R., 2005. Chemical Grouting and Soil Stabilization. CRC Press.

Katgert, G., van Hecke, M., 2010. Jamming and geometry of two-dimensional foams. Europhysics Letters 92, 34002.

Leroueil, S., Vaughan, P., 1990. The general and congruent effects of structure in natural soils and weak rocks. Géotechnique 40, 467–488.

Marques, S., Festugato, L., Consoli, N., 2021. Stiffness and strength of an artificially cemented sand cured under stress. Granular Matter 23.

Mitchell, J., Soga, K., 2005. Fundamentals of Soil Behavior, 3rd Edition. John Wiley.

Ning, Z., Khoubani, A., Evans, T.M., 2017. Particulate modeling of cementation effects on small and large strain behaviors in granular material. Granular Matter 19, 1–19.

Oda, M., 1977. Co-Ordination Number and Its Relation To Shear Strength of Granular Material. Soils and Foundations 17, 29–42.

Ouadfel, H., Rothenburg, L., 2001. 'Stress-force-fabric' relationship for assemblies of ellipsoids. Mechanics of Materials 33, 201–221.

Renouf, M., Dubois, F., Alart, P., 2004. A parallel version of the non smooth contact dynamics algorithm applied to the simulation of granular media. Journal of Computational and Applied Mathematics 168, 375–382.

Robertson, P., Melo, L., Williams, D., Wilson, G., 2019. Report of the Expert Panelon the Technical Causes of the Failure of Feijao Dam. Technical Report. Vale S.A.

Rosa, F., Consoli, N., Baudet, B., 2008. An experimental investigation of the behaviour of artificially cemented soil cured under stress. Géotechnique 58, 675–679.

Rothenburg, L., Bathurst, R., 1989. Analytical study of induced anisotropy in idealized granular material. Géotechnique 39.

Schnaid, F., Prietto, P., Consoli, N., 2001. Characterization of cemented sand in triaxial compression. Journal of Geotechnical and Geoenvironmental Engineering 127, 857–868.

Shen, Z., Jiang, M., Thornton, C., 2016. Dem simulation of bonded granular material. part i: Contact model and application to cemented sand. Computers and Geotechnics 75, 192–209.

Voivret, C., Radjai, F., Delenne, J.Y., El Youssoufi, M., 2007. Space-filling properties of polydisperse granular media. Phys. Rev. E 76, 1–12.

Wang, Y., Leung, S., 2008. Characterization of cemented sand by experimental and numerical investigations. Journal of Geotechnical and Geoenvironmental Engineering 134, 992–1004.

Yimsiri, S., Soga, K., 2010. Dem analysis of soil fabric effects on behaviour of sand. Géotechnique 60, 483–495.